RESEARCH ARTICLE

ADVANCED MATERIALS TECHNOLOGIES
www.advmattechnol.de

Leveraging the Snap Buckling of Bistable Magnetic Shells to Design a Refreshable Braille Dot

*Arefeh Abbasi, Tian Chen, Bastien F.G. Aymon, and Pedro M. Reis**

A design concept is proposed for the building block, a *dot*, of programmable braille readers utilizing bistable shell buckling, magnetic actuation, and pneumatic loading. The design process is guided by Finite Element simulations, which are initially validated through precision experiments conducted on a scaled-up, single-shell model system. Then, the simulations are leveraged to systematically explore the design space, adhering to the standardized geometric and physical specifications of braille systems. The findings demonstrate the feasibility of selecting design parameters that satisfy both geometric requirements and blocking forces under moderate magnetic fields, facilitated by pneumatic loading to switch between the two stable states. While the study is focused on experimentally validated numerical simulations, it is also identify several manufacturing challenges that need to be resolved for future physical implementations .

1. Introduction

Magneto-rheological elastomers (MREs) are a class of active composite materials comprising an elastomeric matrix dispersed with micron-sized magnetic particles.[1,2] Under the application of an external magnetic field, structural elements made of MREs can undergo mechanical deformation, which can be leveraged for function.[1] The general class of MREs can be further subdivided into soft MREs (s-MREs)[3,4] and hard MREs (h-MREs),[5,6] each displaying distinct characteristics in their response to external magnetic fields; s-MREs have low coercivity, while h-MREs show high coercivity in addition to the ability to retain a high level of magnetization. H-MREs, embedded with hard-ferromagnetic particles, can experience significant deformations or rotations by harnessing magnetic torques and forces arising from the magneto-elastic coupling between the material and the applied magnetic field. Over the past decade, this interplay between magnetism and mechanics has received significant attention, paving the way for a spectrum of novel applications across diverse fields, ranging from soft robotics[7–10] and biomedical engineering devices[6] to flexible electronics[11,12] and metamaterials.[13]

Despite recent advances, the predictive design of structural elements and devices using h-MREs remains challenging due to the nontrivial coupling between elastic–magnetic effects and geometric nonlinearities. A continuum theory has been recently developed[5] for the finite deformation of 3D h-MREs through a nonlinear magneto-mechanical constitutive law. Based on this 3D continuum model, dimensional-reduction procedures have been employed to derive structural theories for hard-magnetic beams with "elastica"-like planar deformation,[14,15] rods with 3D deformation,[16] plates,[17] and shells.[18,19]

Shallow shells, with their unique structural characteristics, can exhibit bistable behavior, meaning they possess two stable states.[20] With this ability to maintain stable states until triggered otherwise, bistable shells have found numerous engineering applications for switching,[21,22] locking,[23] or actuation mechanisms.[24,25] The fast transition between these two stable states, also known as "snap-through," can be triggered in different ways, for example, through magnetic loading,[26,27] mechanical loading,[28] or fluid flow.[29]

Serving as a motivation for our study, we will consider the bistable behavior of hard-magnetic shells in the context of the potential application to braille displays.[30] Combining the inherent bistability of shells made of h-MREs with magnetic and mechanical actuation, our vision is that braille displays could be made refreshable through controlled state changes.

In recent years, technological advancements have stimulated the development of refreshable braille displays (RBD) driven by a variety of actuation mechanisms, including piezoelectrics,[31–34] electromagnetics,[35–37] or thermopneumatics.[38] These devices often use advanced materials such as electroactive polymers,[39–42] shape memory alloys,[43–45] or dielectric elastomers.[46,47] Piezoelectric actuators have been favored for commercial RBD due to their fast refresh rates, low power consumption, and reliability, albeit at a relatively high cost.[30–32] Electromagnetic linear actuators tend to have a low ratio between

A. Abbasi, B. F. Aymon, P. M. Reis
Flexible Structures Laboratory
Institute of Mechanical Engineering
École Polytechnique Fédérale de Lausanne (EPFL)
Lausanne 1015, Switzerland
E-mail: preis@mit.edu

T. Chen
Architected Intelligent Matter Laboratory
Department of Mechanical Engineering
University of Houston
Houston, TX 77024, USA

The ORCID identification number(s) for the author(s) of this article can be found under https://doi.org/10.1002/admt.202301344

DOI: 10.1002/admt.202301344

output force and operating velocity, requiring complex packaging and a considerable force to hold a raised dot.[48,49] RBD utilizing shape memory alloys requires intricate heating and cooling processes, posing practical implementation challenges.[33,43,45] Dielectric elastomers have been gaining traction for lightweight tactile displays, offering high actuator density and a wide range of motion, with performance comparable to previous technologies, but in a more compact form.[46,47] However, their required large driving voltages can be impractical for some applications. Most technological solutions for braille readers cannot offer sufficiently high-quality performance, especially regarding the balance between fast shape-changing dynamics and low power consumption.[50] Additionally, the mainstream adoption of advanced tactile displays is hindered by the lack of compact, large-area actuator arrays that can stimulate multiple sensory receptors while adhering to high user-safety standards. Existing solutions tend to be costly and require complex manufacturing processes. Despite ongoing efforts,[51] designing RBD devices that are simple, compact, low-cost, large-scale, user-friendly, and reliable remains challenging.

Here, we propose an alternative design concept for the braille dot, the building block of braille readers, leveraging the buckling and bistability of thin shells fabricated from h-MREs. Inspired by the popular "Pop it" toy,[52] these shells can be reversibly set in a convex or concave state (**Figure 1a**). Each of these shells (dots) can then be arranged in a 3 × 2 matrix and programmed, on-demand, to form a braille symbol. The dots have independent writing and reading phases under magnetic and mechanical loading, respectively. During writing, a transient external magnetic field can induce snap-through buckling to transition the shell between its two stable states: from ON (bump) to OFF (dimple) or vice versa. For reading, shells in the ON state must sustain a blocking force in reaction to the finger indentation without snapping to the OFF state. Methodologically, we follow a computational approach, using state-of-the-art simulations based on the Finite Element Method (FEM). These simulations are first validated against precision experiments on a scaled-up (centimeter-scale) physical model of a braille dot. Then, we study dots at their actual scale, ensuring adherence to standard braille specifications,[53] with a special focus on their geometry, elastic response, and actuation. Although the primary driver of actuation is an external magnetic field, it is supplemented with a transient pneumatic loading to aid in widening the design space. We recognize that scaling down the current design concept, especially in terms of fabrication, will introduce a distinct set of challenges and limitations, including fabrication processes, material properties, and actuation mechanisms within smaller dimensions. We hope that such challenges will be addressed in future work. Still, our systematic exploration of the design space using predictive computational tools enables us to identify the regions that meet the various design constraints, making a step toward a new class of programmable braille displays.

2. Problem Definition: Braille Reader Design Concept

Worldwide, 285 million people experience visual impairments,[54] influencing various aspects of daily life, such as access to printed or digital content. Braille code, a tactile writing system, facilitates these interactions, mapping symbols (e.g., letters and numbers) into arrays of cells, each comprising a 3 × 2 matrix of dots. Each dot can independently be raised or flat, and words are then formed by assembling a series of such cells. Braille users typically read by tracing their fingertips across rows of these cells, whose dimensions are optimized to allow the index finger pad to cover the entire cell and discern each dot.

The specifications for braille cells and dots are standardized by the World Blind Union,[53] and the relevant parameters are required to lie within the following ranges: $\ell_d \in [2.3, 2.5]$ mm for the dot-to-dot spacing, $\ell_c \in [6, 7]$ mm for the distance between two distinct cells, and $\ell_l \in [10, 11]$ mm for the distance between two lines of words. Furthermore, each raised dot must feature a quasi-hemispherical cap with base diameter $D \in [1.4, 1.6]$ mm and height $h \in [0.4, 0.9]$ mm.[55] Finally, to sustain the normal indentation force applied by the index finger during reading, each dot must be able to withstand a minimum blocking force of $F >$ 50 mN.[53]

Our objective is to design a programmable braille dot that adheres to the aforementioned braille specification. We consider a bistable shell clamped at its base (Figure 1a,b). The analysis is segmented into two phases: "*Writing*" (Figure 1c) and "*Reading*" (Figure 1d). For writing, the ON-OFF switching is done via magnetic actuation. Concurrently with this phase, we temporarily depressurize the shell to lower the energy barrier required for buckling. By contrast, during the reading phase, the shell is pressurized to increase its rigidity. We seek to identify the key design variables and protocols required for the fabrication and operation of our system. Next, we describe the geometric considerations and the two operational phases.

The geometry of our model braille-dot (Figure 1a) comprises a shell of diameter $D = 1.45$ mm and height $h = 0.48$ mm, in accordance with braille standards. This shell is fabricated by the buckling of a radially compressed circular plate (thickness t) made of h-MRE[17] when the in-plane pre-stretch, λ, of two boundary annuli is released (Figure 1b), as detailed in Section 6. One first goal of the design is to select appropriate values of t and λ that, upon buckling of the plate, yield a shell with the target value of h, satisfying braille requirements.

For the writing phase (Figure 1c), we will characterize the snap buckling of the shells under loading by a uniform magnetic field, $\mathbf{B}^a_c$, to switch between their two stable states. We assume that each dot, which would eventually form the 3 × 2 cell, can be actuated independently. For the present study, we restrict our focus to the operation of a single dot. The goal of this design phase is to identify the critical magnetic field, B^a_c, required for snapping under the limitation set by upper-bound of the linear regime of the **B**-**H** hysteresis curve for the h-MRE material[5] (additional details are provided in Section 6). Subsequently, we aim to determine the corresponding geometric and fabrication parameters, t, and λ, that yield the desired snap-buckling characteristics.

For the reading phase (Figure 1d), the braille dots must be designed such that the user can tactilely discern the dots without altering their state. The challenge lies in ensuring that a dot in the ON state can sustain the indentation force mentioned above ($F \geqslant 50$ mN) without snapping to the OFF state, thereby inadvertently erasing the braille pattern. This design phase targets the determination of optimal geometric and fabrication parameters

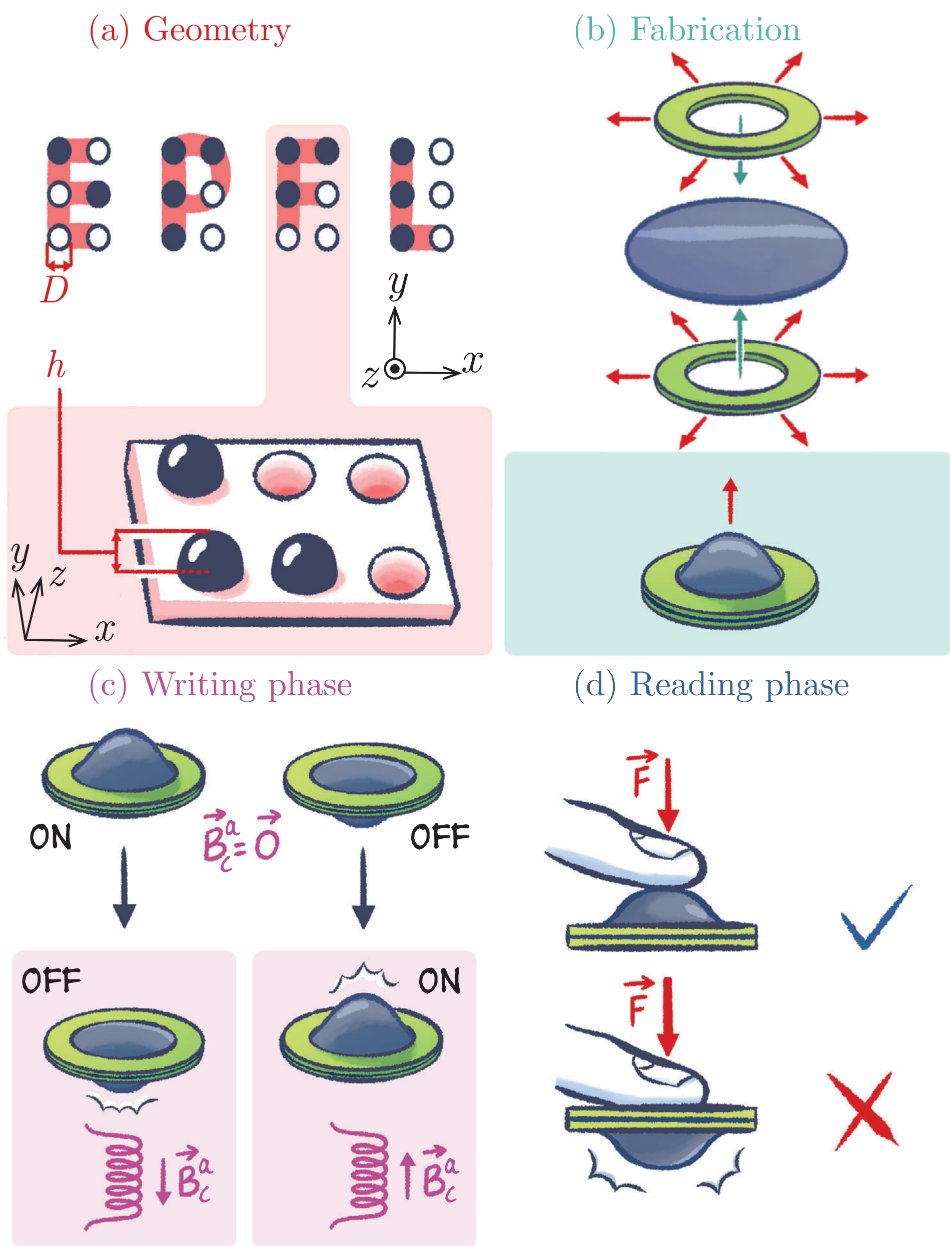

Figure 1. Design, fabrication, and operation of a bistable Braille dot. a) Geometry: A word is formed by assembling a series of braille cells, each comprising 3 × 2 dots. "EPFL" is shown as an example. b) Fabrication: A bistable shell is fabricated by sandwiching a circular h-MRE plate between two radially pre-stretched boundary annuli. This pre-stretch is then released to buckle the plate into a shell. c) Writing phase: an external magnetic field, $\mathbf{B}^a$, sets each shell in one of its two stable states, either ON (bump) or OFF (dimple). d) Reading phase: an index finger applies an indentation force, F on each dot.

for the dot, specifically its thickness t and pre-stretch λ, to meet this requirement.

The constraints associated with the fabrication protocol and the ensuing dot geometry, coupled with the requirements for the reading and writing phases, underscore the intricacies involved with designing our braille dot. We aim to identify the feasible design parameter space of the system (specifically, t and λ) that satisfies the constraints on h, F, and B^a_c. This design exploration will be performed solely using FEM simulations, which will be initially validated against experiments in a scaled-up system.

3. Results and Discussion

3.1. Validation of the FEM Simulations Against Experiments

We first validate the FEM simulations (technical details are provided in Section 6) against experiments (see Section 6) on the scaled-up model system, considering the results from the geometry characterization of the fabricated shells, as well as from the reading and writing experiments.

During sample fabrication, the buckling of the plate, which yields a shell, may produce undesirable wrinkling patterns.[56]

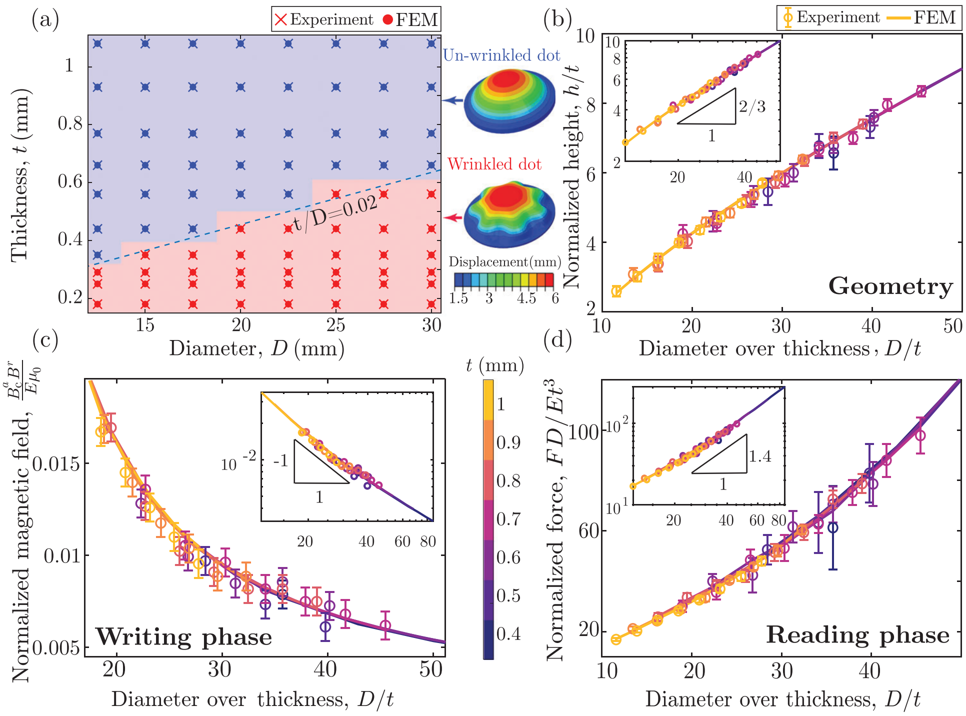

Figure 2. Validation of FEM simulations against the scaled-up experiments. a) Phase diagram in the (t, D) parameter space. The experiments and simulations correspond to the cross and circle symbols, respectively. The smooth and wrinkled shells are represented by the blue and red symbols, respectively; the empirical phase boundary between the two is represented by the dashed line. The normalized b) shell height, h/t, c) critical magnetic field, $B_c^a B^r/(E\mu_0)$, and d) blocking force, $FD/(Et^3)$ are plotted as functions of the normalized base diameter of the shell, D/t, for ten different values of thickness, t. The error bars of the experimental data represent the standard deviation of six independent measurements on the same specimen. The different values of t are color-coded (see adjacent color bar). The solid lines and data symbols correspond to FEM and experiments, respectively. The insets show the log-log plots of the data. Throughout, the fabrication pre-stretch is $\lambda = 0.1$.

To act as braille dots, ideal shells should be smooth (i.e., free of these wrinkles). Toward identifying the design space for these ideal shells, **Figure** 2a presents a phase diagram of the thickness-diameter parameter space (t, D) for representative shells fabricated with a pre-stretch of $\lambda = 0.1$ (see Sections 6, and 6). There is excellent agreement between experiments (crosses) and FEM (circles), serving as a first step in validating the simulations. Wrinkling is observed for higher values of the slenderness ratio D/t. For the chosen pre-stretch ($\lambda = 0.1$), the empirical phase boundary between ideal and wrinkled shells is $t \approx 0.02D$ (dashed line).

First, focusing on the geometry characterization, Figure 2b plots the normalized height, h/t, of the smooth shells (blue region in Figure 2a) versus D/t. The FEM simulations (lines) and experimental data (symbols) are obtained with a fabrication pre-stretch of $\lambda = 0.1$ and thickness in the range $t \in [0.18, 1.08]$ mm (see Section 6). The data collapses onto a single curve, with excellent agreement between experiments and FEM, thereby validating the FEM for the shell fabrication. Moreover, the inset of Figure 2b shows that the relation between h/t and D/t is a power-law with an exponent of $\approx 2/3$[57,58]

Toward validating the writing-phase simulations, in Figure 2c, we plot the normalized magnetic field required for snapping, $B_c^a B^r/(E\mu_0)$, as a function of D/t, where E is Young's modulus, μ_0 is relative permeability of air, and B^r is the residual magnetic flux density. Naturally, increasingly slender shells require a lower magnetic field for snapping, and the data collapse into a single curve, exhibiting a power law with an exponent ≈ -1. This scaling originates from the balance between magnetic and elastic energies investigated in our previous work,[18,19] which suggests $B_c^a B^r/(E\mu_0) \sim (D/t)^{-1}$; a prediction in agreement with our present data (inset of Figure 2c).

In Figure 2d, we present the results for the reading, plotting the normalized blocking force, $FD/(Et^3)$ (required to snap the shell), as a function of D/t. Again the experiments (symbols) are in excellent agreement with the FEM (lines). The data is consistent with a power law with exponent ≈ 1.5, which can be rationalized using well-established results for the indentation of a spherical shell by a flat plate, causing mirror buckling (to produce an inverted cap) of the shell.[59–62] Balancing the stretching and bending energies of the shell, the dimensionless indentation force is expected to scale as $FD/(Et^3) \sim (D/t)^{3/2}$, a prediction that is consistent in our data (inset of Figure 2d). For completeness, the dimensional version of the plots shown in Figure 2b–d are provided in Section S1 (Supporting Information).

Overall, we found excellent agreement between the experiments and the FEM simulations of the scaled-up model system for the shell-fabrication protocol and their geometric characterization, as well as for the reading and writing phases.

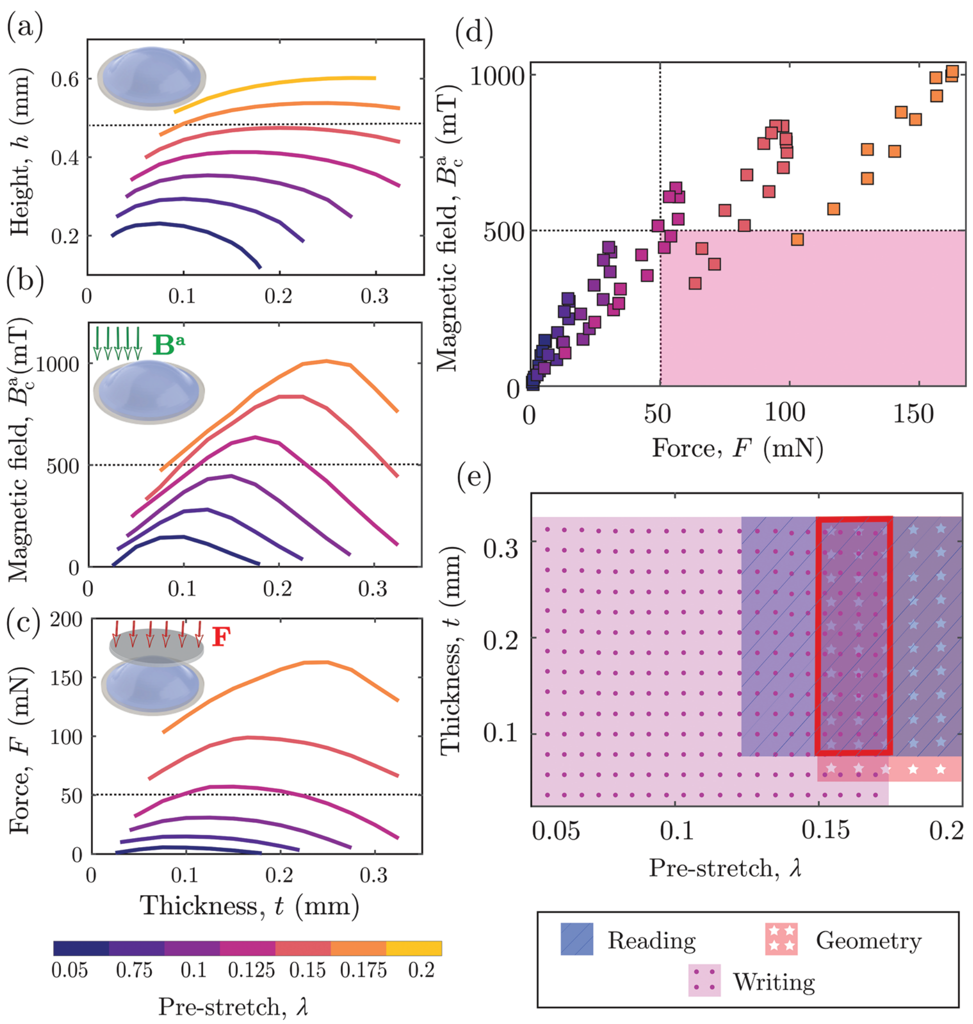

Figure 3. Design of the real-scale braille dot. The a) dot height, h, b) critical magnetic field, B_c^a, and c) blocking force, F, are all plotted versus thickness, t, at different levels of pre-stretching, $\lambda = [0.05, 0.2]$ (increments of 0.05). The horizontal dashed lines represent the design constraints of the corresponding quantities. d) Phase diagram in the (B_c^a, F) parameter space, with the desired shaded region. e) Phase diagram in the (t, λ) parameter space for the geometry step and reading and writing phases, with the feasible design space indicated by the rectangle region. All results were obtained from FEM simulations.

3.2. Design of At-Scale Braille Dots

We shift our attention from the scaled-up model system to investigate the design of the real-scale braille dots. Leveraging the FEM simulations validated above and following the protocol details in Section 6, we explore the design space for braille dots and determine their optimal fabrication and operational conditions. Each dot must conform to the specifications laid out in Section 2. Our objective is to determine the optimal ranges for the key geometrical parameters (thickness, t, and fabrication pre-stretch, λ) that simultaneously meet the acceptable design constraints for dot height (obtained from fabrication) and meet feasible operational conditions for the writing phase (critical magnetic field for actuation), and reading phase (blocking force). Finally, we will identify the intersecting region of these three design sub-spaces.

First, we characterize the geometry of the dots obtained from the fabrication step of the simulations. In **Figure** 3a, we plot the dot height, h, versus thickness, t, for different levels of λ. The color map represents the various levels of λ, whose range is specified in Section 6. The resulting $h(t)$ curves exhibit a non-monotonic trend, with overall values (including the maximum of the curves) that increase with λ. This non-monotonic behavior arises because, for either very thick or thin plates, the pre-stretch release (compression) leads to planar (radial) contraction rather than increasing the out-of-plane deformation of the buckled plate (shell). The horizontal dashed line represents the minimum dot height, $h \geqslant 0.48\,mm$, required by braille specifications. Thus, to satisfy this requirement, we find that the feasible range for the fabrication pre-stretch is $\lambda \geqslant 0.15$, and the viable thickness range is $t \in [0.05, 0.325]$ mm.

Next, we consider the writing phase, which enables the braille dot (magnetic shell) to switch between its two stable stages. In Figure 3b, we plot the critical amplitude of the magnetic field, B_c^a, required to snap the dot as a function of t, for different fabrication pre-stretches. We observe that, B_c^a increases with λ (and thus for taller dots; cf. Figure 3a), also with a non-monotonic dependence on t. To prevent the demagnetization of the shell due to high magnetic fields,[5] we established the upper limit $B_c^a \leq 500$ mT, represented by the horizontal dashed line in Figure 3b). Consequently, for actuation within this magnetic-field limit, the allowed parameters are in the ranges $t \in [0.025, 0.325]$ mm, and $\lambda \in [0.05, 0.175]$.

Finally, we turn our attention to the reading phase. In Figure 3c, we plot the blocking force, F, as a function of t, using the same ranges of the other parameters which are specified in Section 6. Increasing λ leads to an overall increase of the $F(t)$ curves, much like the writing phase, which is also non-monotonic. Combining these results with the $h(t)$ data in Figure 3a implies that taller dots require a higher indentation force for inversion, presumably due to their geometry-induced rigidity.[63,64] According to braille specifications, the blocking force of the dot must be at least $F \geqslant 50$ mN (horizontal dashed line in Figure 3c), which is limited by the potential snapping of the shell due to the touch by a fingertip. Under this constraint, we determine that the ranges of feasible parameters for this reading phase are $t \in [0.075, 0.325]$ mm, and $\lambda \geqslant 0.125$.

Combining the above results for the viable ranges of the parameter space (t, λ) dictated by the geometry characterization, writing, and reading phases, we present the intersection of these three design phases in Figure 3d. At each level of λ (colored symbols), we plot B_c^a as a function of F for all the thickness values. An overall correlation emerges between B_c^a and F. In the plot, the design constraints on B_c^a and F mentioned above are represented by the shaded region, which only intersects with a few of the explored designs ($\lambda \geqslant 0.125$). The design constraints require a sufficiently high blocking force while ensuring a sufficiently low magnetic field, a trade-off that is challenging to achieve in our system.

In Figure 3e, we present an alternative version of the overlap of all of the design constraints explored above, now in the final target design parameter space (t, λ). Each separate shaded/textured region relates to the individual viable bounds obtained above for the geometric characterization, writing, and reading phases. Meeting all the constraints and ensuring braille standards requires an overlap of these three regions; i.e., the domain enclosed by the dashed rectangle with $t \in [0.1, 0.325]$ mm and $\lambda \in [0.15, 0.175]$.

3.3. Design Improvement using a Pneumatic System

The feasible design space identified from the results in the previous section is rather limited, making a flexible fabrication process challenging. The design requires the shell to be able to snap during the writing phase yet remain resistant to snapping during the reading phase. To address these conflicting limitations without altering the geometry, we propose the incorporation of an additional pneumatic loading system. This pneumatic component modulates the energy barrier for buckling in both the reading and writing phases; the pressure difference, ΔP, between the inside and outside of the dot is positive for the reading phase and negative for the writing phase. The implementation details of this pneumatic loading in the FEM simulations are provided in Section 6. Hereon, we focus on shells fabricated with a pre-stretch of $\lambda = 0.15$, which was deemed practical from the parameter exploration presented above.

For the writing phase, the dot is depressurized to reduce the critical magnetic field B_c^a required for snapping, thereby facilitating the switching of the dot. In **Figure 4a**, we plot B_c^a versus ΔP, for different values of t. The results show that applying pneumatic loading substantially reduces the magnetic field B_c^a. The $B_c^a(\Delta P)$ curves are linear, with a slope that varies with t. For example, depending on t, a dot depressurized by $\Delta P \lesssim -60$ kPa can lower the critical magnetic field for snapping by as much as 50%, compared to the zero-pressure case. The horizontal dashed line represents the maximum acceptable magnetic field.

For the reading phase, in contrast to the writing phase, the dot is pressurized to enhance the blocking force, F, and better resist indentation. The dot is first pressurized and then loaded at its pole. In Figure 4b, we present the dependence of the blocking force F on the applied ΔP for different thickness values, t (see adjacent color bar). In the explored range of parameters, the $F(\Delta P)$ response is linear, as expected from previous work,[63,64] and no buckling occurs. For example, the resistance of the dot to indentation force can be increased by up to 100% (at $t = 0.2$ mm) compared to the zero-pressure case. We find that all curves are now well above the 50 mN limit imposed by braille standards.

Finally, in Figure 4c, we combine data from both phases with pneumatic loading (Figure 4a,b) and plot B_c^a versus F. The shaded region indicates the viable range of parameter space; with a pneumatic load of $|\Delta P| \geqslant 40$ kPa, we achieve successful reading and writing operations across the full thickness range. The limit values of $|\Delta P|$ could be further tuned by varying the fabrication pre-stretch λ, but we leave a more systematic exploration for future work. Our results demonstrate that using this additional pneumatic component, the design space of the system is significantly expanded compared to the zero-pressure case explored in Section 3.2.

4. Expected Challenges to Fabricate At-Scale Braille Dots

The focus of the present mechanics-based study is on proposing a design concept for a switchable braille dot and exploring its feasible parameter space using predictive computational tools. Still, in this section, we discuss some potential challenges and limitations expected to be encountered during the miniaturization and fabrication of at-scale dots for actual implementation in concrete applications.

Scaling down the proposed design concept, especially in terms of fabrication, should introduce a distinct set of challenges than those encountered in our model centimeter-scale experiments, whose purpose was to validate the FEM simulations. These expected challenges include the details of the actual fabrication processes, material properties, and actuation mechanisms within smaller dimensions. In terms of fabrication, achieving the level of precision desired for the dot fabrication, based on the release of stretch in the pre-stretched plate, may be difficult to implement at the sub-millimeter scale, and the miniaturized components may require specialized manufacturing processes. Furthermore, given that the size of the magnetic particle we used in the fabrication of the MRE material was ≈ 5μm, achieving at-scale

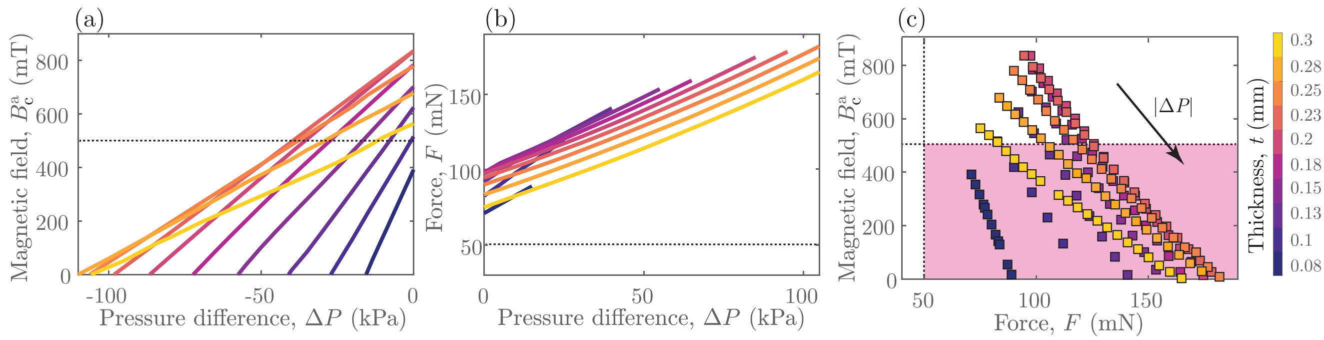

Figure 4. Improved design of real-scale braille dots with pneumatic system. a) Blocking force, F, and b) magnetic field, B_c^a, plotted as a function of the pressure difference, ΔP. The thickness was varied in the range $t = [0.075 - 0.3]$ mm (in increments of 0.025 mm) for a specific pre-stretch $\lambda = 0.15$. The horizontal dashed lines represent the limiting bounds imposed by the braille standards. c) Phase diagram in the (B_c^a, F) parameter space with the desired regions of viable parameters (shaded region), for different levels of pressure difference, $0 < |\Delta P| < 120$ kPa. All results were obtained from FEM simulations.

dots with homogeneous thickness may require the usage of magnetic nanoparticles.

In addition, generating the required magnetic field and enabling actuation of the braille dot at the real scale will call for the development of custom-designed electromagnetic coils. Even if, in practice, we believe that this will be a non-trivial task, in Section S2 (Supporting Information), we demonstrate that, in principle, it is feasible. Specifically, we have performed simulations using COMSOL of the magnetic field generated by an electromagnet (solenoid) under the design constraints imposed by the actual scale of a braille dot. Our results show that it is reasonable to expect to generate magnetic fields of the magnitude of $B_{\text{max}} \approx 200$ mT, which is within the range required for the operation of the braille dot (cf. Figure 4). Actual practical implementations of our proposed design will likely have to tackle other concrete, practical challenges, including the potential heterogeneity of the magnetic field, that go beyond the scope of the present study.

5. Conclusion

We have proposed a new design concept for a reversibly switchable braille dot as a building block for refreshable braille displays. The proposed mechanism uses bistable magnetic shells that can be snapped on-demand under an external magnetic field (writing phase) while resisting buckling due to the indentation by a fingertip (reading phase). An additional pressure-loading component expands the available design space without modifying the dot geometry. First, we performed experiments on a scaled-up model system to validate FEM simulations. These simulations were then leveraged to systematically explore the design space at realistic scales while meeting braille standards (geometry and tactile sensitivity) with reasonable magnetic field strengths and temporary pneumatic loading. Our design boasts several advantages over existing solutions, including bistability for self-stabilization, as well as fast state-switching and pattern refreshment. This switching can be triggered by a transient magnetic field rather than a continuous energy input. Finally, a constant pneumatic input for the whole actuator enables the tuning of the power input of the system.

While our design introduces promising advances, it is not without potential limitations. Its complexity calls for advanced manufacturing and assembly techniques. Miniaturized solenoids to generate the required magnetic field under each dot would need to be developed. Furthermore, incorporating a hybrid magnetic and pneumatic system could pose challenges in terms of size and power, particularly for portable or battery-operated devices. Despite these potential obstacles, we anticipate that future research and physical implementation of this concept could make it possible to build a new class of compact, user-friendly, and cost-effective braille readers.

6. Experimental Section

Experiments with the Scaled-Up System: In this section, the fabrication protocol, geometric characterization, and testing (writing and reading phases) are detailed for the experiments on the scaled-up model system. The data obtained from these experiments serve to validate the FEM simulations in Section 3.1.

Fabrication: An established experimental procedure was followed to prepare the h-MRE material used to fabricate the specimens.[15,17,28] First, Vinylpolysiloxane (VPS-32, Elite Double, Zhermack) was mixed with NdPrFeB particles (MQFP-15-7-20065-089, Magnequench), with volume fraction $c_v = 18.7\%$. Then, an automated film applicator (ZAA 2300, Zehntner) spread the VPS-NdPrFeB mixture into a thin film, which, upon curing, yielded a thin elastic plate. By modulating the gap height of the film applicator, ten plates with thicknesses in the range $t = [0.180, 1.080]$ mm were fabricated, measured using an optical microscope (VHX-950F, Keyence). Post-curing, eight circular plates (**Figure 5a**) were cut with diameters in the range $D_p = [25, 60]$ mm, in increments of 5 mm.

Magnetization: Then, various steps were involved in the magnetization of the magnetic plate, as illustrated in the schematic diagrams in Figure 5a–d. The cut circular h-MRE plate of diameter D_p from the fabricated plate (Figure 5a) did not possess any magnetic properties. Therefore, to magnetize the plate, it was folded symmetrically into a semicircle along x-axis (Figure 5b) and then into a quarter-circle along y-axis (Figure 5c). Third, the folded quarter-circle plate was placed in the impulse magnetizer (IM-K-010020-A, flux density ≈4.4 T, Magnet-Physik Dr. Steingroever GmbH) at an angle of $\alpha = 45°$ with respect to the positive y axis, aligned with the edge of the quarter circle (Figure 5d). The magnetizer generated a magnetic field of strength **B**, inducing a permanent magnetic dipole in the NdPrFeB particles. Assuming a uniform particle dispersion

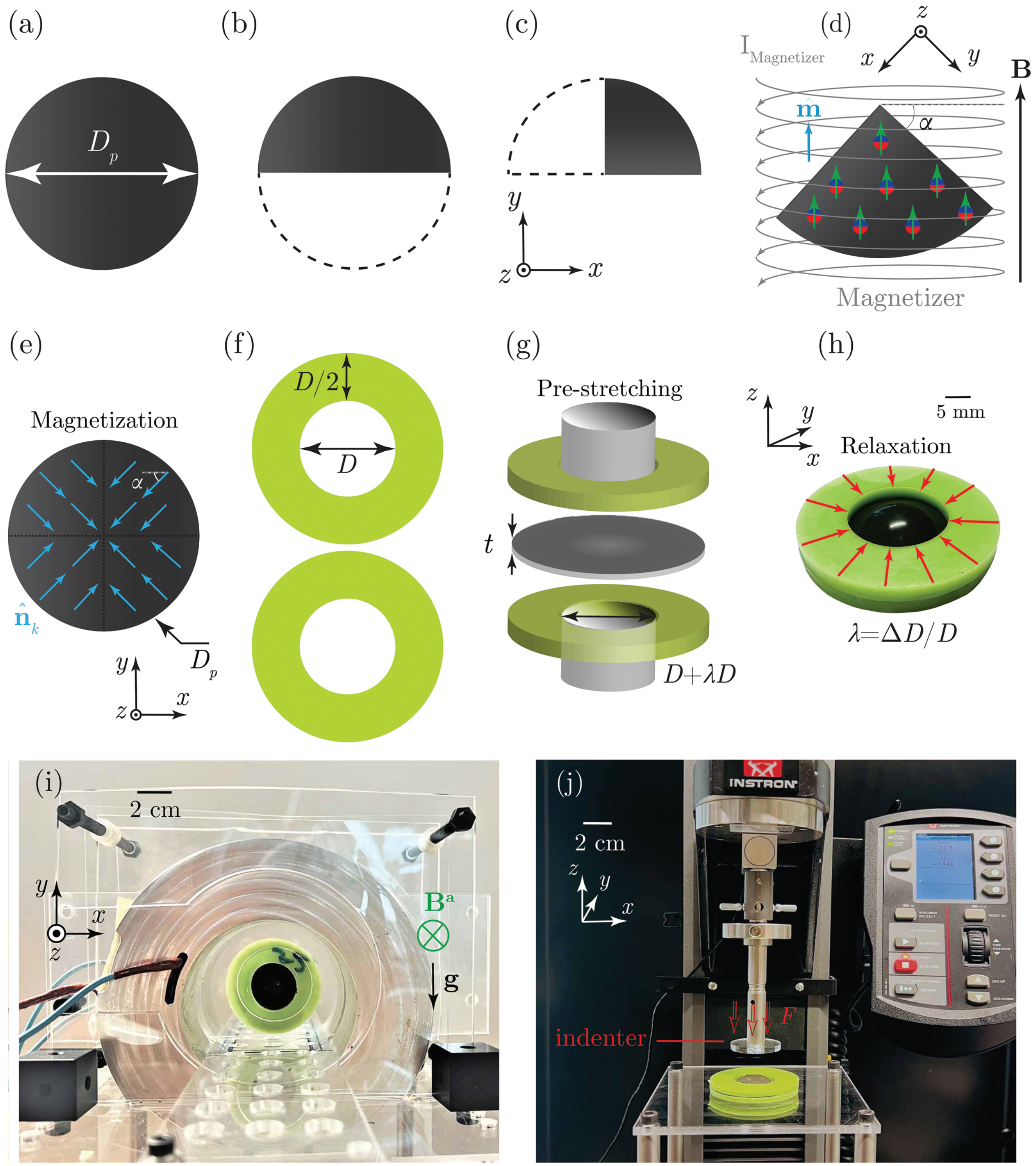

Figure 5. Fabrication and experimental apparatus for the scaled-up model. a) A circular magnetic plate (diameter of D_p) is first b) folded along the *x*-axis and then c) along the *y*-axis to form a quarter-circle shape. d) The folded plate is inserted into the pulse magnetizer at an angle $\alpha = 45°$. The magnetizer generates a strong axial magnetic field, B, which induces a magnetic moment, $\mathbf{m}$. e) The circular h-MRE plate was magnetized while folded, yielding the magnetization profile described by Equation (1). f) Two VPS annuli serve to constrain the plate boundary. g) Cylinders pre-stretched the annuli, which sandwich the h-MRE plate. h) Upon release of the pre-stretch, the plate buckles to form a shell. i) Photograph of the apparatus for the *writing* experiments. The shell is placed between two Helmholtz coils and loaded by a uniform magnetic field along $\hat{\mathbf{z}}$. j) Photograph of the apparatus for the *reading* experiments; a plate indents the shell, and the blocking force F is measured.

within the polymer matrix, the magnetization magnitude computed from the volume average of the total magnetic moment of the individual particles is $M = \mu_0{}^{-1}B^r = 134.4$ kAm^{-1}, where B^r is the residual magnetic flux density and μ_0 the relative permeability of air. After unfolding, the magnetization pattern of the circular plate was fourfold symmetric (Figure 5e). In each of the plate's four quarters, $k = \{1, 2, 3, 4\}$, the magnetization is expected to be $\mathbf{M} \approx M\hat{\mathbf{n}}_k$, pointing along the unit vector:

$$\hat{\mathbf{n}}_k = -\cos(\alpha + (k-1)\pi/2)\hat{\mathbf{e}}_x - \sin(\alpha + (k-1)\pi/2)\hat{\mathbf{e}}_y, \quad (1)$$

where $\alpha = 45°$ is the orientation of the folded plate in the magnetizer (see Figure 5d).

Empirically, it was found that the chosen magnetization profile was more effective in inducing snap buckling than simpler patterns (e.g., uniform magnetization parallel or perpendicular to the plate mid-surface). The choice aligned with the anti-symmetric profile selected in recent snap-buckling studies of h-MRE beams.[28,65] It was also acknowledged that the choice of the magnetization profile was motivated by fabrication simplicity. However, the need to conduct a more systematic exploration of other profiles[66] in future research was recognized.

Having fabricated and magnetized the plates, shallow shells were produced through radial compression of the said plates. First, two VPS-32 annuli were fabricated to act as the clamped boundary of the shell, each with inner and outer diameters of $D = D_p/2$ and $2D = D_p$, respectively (Figure 5f). Next, these annuli were stretched using two rigid cylinders of diameter $D + \lambda D$ (Figure 5g), resulting in the radial pre-stretch of $\lambda = \Delta D/D$ (Figure 5g). The plate was then sandwiched and bonded between the annuli using the same VPS material. After curing, the cylinders were removed, thereby relaxing the pre-stretched. Consequently, the plate buckled out-of-plane due to the in-plane (x-y) radial compression, yielding a shell, the braille dot (Figure 5h). The height, h, of this newly formed shell was measured using an optical profilometer (VR-3200, Keyence Corporation).

For the "writing experiments" (Figure 5i), the sample designated for testing was placed within the region of the uniform magnetic field produced by a set of Helmholtz coils.[15,18,28] The sample was clamped between two acrylic (rigid) plates. Gravitational effects were minimized by orienting the shell's snapping direction (along $\pm\hat{\mathbf{z}}$) perpendicularly to gravity (-g$\hat{\mathbf{y}}$). The critical magnetic field B^a_c needed for snap-buckling was determined, thereby writing the desired state of the braille dot. To do so, the magnetic flux density was gradually increased by increasing the current I in the coils, in increments of 0.05 A over 20 s intervals, until snap-through occurred.[28] Additionally, given the symmetric nature of the bistable magnetic dot, erasing was expected to mirror the writing process under the assumption of a uniform magnetic field.

For the "reading experiments," the apparatus shown in Figure 5j was used. The specimen was mounted on an acrylic plate containing a hole to equalize the in-out differential pressure. The shell equator was clamped using its thick boundary annuli and mounted onto an acrylic plate using silicone glue. For the intender, a rigid acrylic disk of diameter $D_{ind} = 0.8D$ was used, smaller than the inner diameter (D) of the thick annular boundary to prevent contact with the perimeter during indentation. The indentation displacement was imposed at a constant velocity, 0.06 mms^{-1}. The reaction force, f, exerted on the indenter was measured by a load cell (2530-5N, Instron). The *blocking force*, F, was defined as the maximum of f, beyond which the shell undergoes snap-through buckling, altering the state of the dot.

Finite Element Modeling Simulations: The FEM simulations were conducted using the commercial package ABAQUS/Standard, undertaking two distinct series of simulations with the same protocol but different parameters. First, the same parameters were worked as the scaled-up model system described in Section 6. The objective was to validate the FEM simulations against experiments. For the second series of simulations, the work shifted to the realistic dimensions of the braille dots discussed in Section 2. In this case, the plate thickness was varied in the range $t = [0.025, 0.325]$ mm (increments of 0.025 mm), and the fabrication pre-stretch of the magnetic plate in the range $\lambda = [0.05 - 0.2]$ (increments of 0.025).

The initially flat, circular magnetic plate was modeled as a three-dimensional solid body. Geometric nonlinearities were accounted for throughout the analysis. Similarly to the experiments, the plate was segmented into four quadrants, each with a magnetization oriented along $\mathbf{n}_k$ (cf Section 6, Equation (1) and Figure 5e). The magnetic plate was discretized using the user-defined 8-node brick element proposed by Zhao *et al.*[5] for the modeling of hard-magnetic deformable solids under a uniform magnetic field. A convergence study was conducted to determine the appropriate level of mesh discretization, resulting in 6 elements in the thickness direction, 60 elements along the diameter, and 200 elements circumstantially. Mechanical loads, both contact (indentation) and distributed (pressure), were applied via a dummy mesh of C3D8R solid elements sharing the same nodes as the user elements. The material was assumed to be an incompressible ($\nu \approx 0.5$) Neo-Hookean solid with a bulk modulus 100 times higher than its shear modulus ($G = E/3$) and a Young's modulus of $E = 1.76$ MPa.

In both the scaled-up and real-scale simulations, various combinations of the parameters (t, D, λ) were explored to investigate (1) geometry of the fabricated dot (Figure 1b), (2) writing phase (Figure 1c), and (3) reading phase (Figure 1d), as specified next.

(1) *Geometry*: To account for the possible emergence of higher-order modes during plate buckling, the entire magnetized plate was simulated without any symmetry assumptions (cf. Section 6). In order to break the symmetry on the $x - y$ plane and induce buckling, a small out-of-plane displacement ($0.01t$) was applied as an initial perturbation. Then, the Dirichlet boundary condition was specified on each boundary node and compression was applied by imposing radially inward-directed displacements toward the center of the plate, a process that led to the formation of the shell. The extent of compression was set through λ.
(2) *Writing*: For the writing-phase simulations, having set the dot geometry in step (1), the raised dot (ON state) was subjected to a uniform external magnetic field, $B^a = 1$ T. The field was applied with a slight misalignment of 1° about the -$\hat{\mathbf{z}}$ direction to trigger asymmetrical buckling modes, thus providing a closer approximation of actual experimental conditions. The magnitude of the magnetic field was then increased linearly in the range of [0, 1] T. The magnetic field magnitude, B^a_c, needed to snap the dot to the second stable state, was determined from the magnetic-field increment at which the displacement of the shell pole exhibited a sudden jump.
(3) *Reading*: For the reading-phase simulations, the indentation was simulated using a rigid circular plate indenter that exerted controlled displacements and discretized using rigid elements. The contact between the indenter and the shell was assumed to be hard and frictionless, thereby preventing surface penetration and sliding. To quantify the mechanical force needed to induce snapping, the dots were subjected to a downward indentation load (along $-\hat{\mathbf{z}}$) until reversal occurred, and the blocking (maximum) force, F, was recorded.
(4) *Pneumatic loading*: When simulating the real-scale braille dots, a constant pneumatic load was also considered, as discussed in Section 3.3. This pressure loading served to widen the design space by stiffening the dot against snapping during the reading phase (indentation) and reducing the energy barrier during the writing phase. For each dot geometry, first, the critical pressure, P_{cr}, required to snap the shell on its own was measured, following the same procedure used to measure the critical magnetic field for snapping.[18,67] A constant positive (or negative) pressure difference, within the range $|\Delta P| \in [0, P_{cr})$ (in increments of 1 kPa) was applied normally to the surface of the shell before initiating the reading (or writing) simulation steps, respectively. Steps (2) and (3) described above were repeated under this constant pneumatic loading. Finally, the blocking force, F, and the critical magnetic field amplitude, B^a_c, were recorded for each pair of parameters (ΔP, t). For these simulations, we set the fabrication pre-stretch to $\lambda = 0.15$.

Supporting Information

Supporting Information is available from the Wiley Online Library or from the author.

Acknowledgements

The authors are grateful to Dong Yan for fruitful discussions and Naïs Coq for providing the illustration of Figure 1. A.A. acknowledges funding from the Federal Commission for Scholarships for Foreign Students (FCS) through a Swiss Government Excellence Scholarship (Grant No. 2019.0619).

Conflict of Interest

The authors declare no conflict of interest.

Data Availability Statement

All data used or plotted in this study is provided as Supplementary Information.

Keywords

bistability, braille reader, magneto-rheological elastomers, shell buckling

Received: August 15, 2023
Revised: November 24, 2023
Published online:

[1] S. Samal, M. Škodová, L. Abate, I. Blanco, *Appl. Sci.* **2020**, *10*, 4899.
[2] T. Miyazaki, H. Jin, *The Physics of Ferromagnetism*, vol. *158*, Springer Science & Business Media, Springer Berlin, Heidelberg, **2012**.
[3] J. Ginder, S. Clark, W. Schlotter, M. Nichols, *Int. J. Mod. Phys. B* **2002**, *16*, 2412.
[4] K. Danas, S. Kankanala, N. Triantafyllidis, *J. Mech. Phys. Solids* **2012**, *60*, 120.
[5] R. Zhao, Y. Kim, S. A. Chester, P. Sharma, X. Zhao, *J. Mech. Phys. Solids* **2019**, *124*, 244.
[6] Y. Kim, G. A. Parada, S. Liu, X. Zhao, *Sci. Rob.* **2019**, *4*, eaax7329.
[7] H.-W. Huang, M. S. Sakar, K. Riederer, N. Shamsudhin, A. Petruska, S. Pané, B. J. Nelson, in *2016 IEEE International Conference on Robotics and Automation (ICRA)*, IEEE, **2016**, pp. 1719–1724.
[8] W. Hu, G. Z. Lum, M. Mastrangeli, M. Sitti, *Nature* **2018**, *554*, 81.
[9] H. Gu, Q. Boehler, H. Cui, E. Secchi, G. Savorana, C. De Marco, S. Gervasoni, Q. Peyron, T.-Y. Huang, S. Pane, A. M. Hirt, D. Ahmed, B. J. Nelson, *Nat. Commun.* **2020**, *11*, 2637.
[10] L. Pancaldi, P. Dirix, A. Fanelli, A. M. Lima, N. Stergiopulos, P. J. Mosimann, D. Ghezzi, M. S. Sakar, *Nat. Commun.* **2020**, *11*, 6356.
[11] Y. Yan, Z. Hu, Z. Yang, W. Yuan, C. Song, J. Pan, Y. Shen, *Sci. Rob.* **2021**, *6*, eabc8801.
[12] Y. Kim, X. Zhao, *Chem. Rev.* **2022**, *122*, 5317.
[13] T. Chen, M. Pauly, P. M. Reis, *Nature* **2021**, *589*, 386.
[14] L. Wang, Y. Kim, C. F. Guo, X. Zhao, *J. Mech. Phys. Solids* **2020**, *142*, 104045.
[15] D. Yan, A. Abbasi, P. M. Reis, *Int. J. Solids Struct.* **2021**, 111319.
[16] T. G. Sano, M. Pezzulla, P. M. Reis, *J. Mech. Phys. Solids* **2022**, *160*, 104739.
[17] D. Yan, B. F. Aymon, P. M. Reis, *J. Mech. Phys. Solids* **2023**, *170*, 105095.
[18] D. Yan, M. Pezzulla, L. Cruveiller, A. Abbasi, P. M. Reis, *Nat. Commun.* **2021**, *12*, 1.
[19] M. Pezzulla, D. Yan, P. M. Reis, *J. Mech. Phys. Solids* **2022**, *166*, 104916.
[20] M. Taffetani, X. Jiang, D. P. Holmes, D. Vella, *Proc. R. Soc. A: Math., Phys. Eng. Sci.* **2018**, *474*, 20170910.
[21] M. T. A. Saif, *J. Microelectromech. Syst.* **2000**, *9*, 157.
[22] P. Rothemund, A. Ainla, L. Belding, D. J. Preston, S. Kurihara, Z. Suo, G. M. Whitesides, *Sci. Rob.* **2018**, *3*, eaar7986.
[23] X. Hou, Y. Liu, G. Wan, Z. Xu, C. Wen, H. Yu, J. X. Zhang, J. Li, Z. Chen, *Appl. Phys. Lett.* **2018**, *113*, 22.
[24] R. L. Harne, K.-W. Wang, *Harnessing bistable structural dynamics: for vibration control, energy harvesting and sensing*, John Wiley & Sons, Hoboken, NJ, **2017**.
[25] T. Chen, O. R. Bilal, K. Shea, C. Daraio, *Proc. Natl. Acad. Sci. U.S.A.* **2018**, *115*, 5698.
[26] E. Loukaides, S. Smoukov, K. Seffen, *Int. J. Smart Nano Mater.* **2014**, *5*, 270.
[27] K. A. Seffen, S. Vidoli, *Smart Mater. Struct.* **2016**, *25*, 065010.
[28] A. Abbasi, T. G. Sano, D. Yan, P. M. Reis, *Philos. Trans. R. Soc., A* **2023**, *381*, 20220029.
[29] G. Arena, R. MJ Groh, A. Brinkmeyer, R. Theunissen, P. M. Weaver, A. Pirrera, *Proceedings of the Royal Society A: Mathematical, Physical and Engineering Sciences* **2017**, *473*, 20170334.
[30] D. Leonardis, L. Claudio, A. Frisoli, in *International Conference on Applied Human Factors and Ergonomics*, Springer, **2017**, pp. 488–498.
[31] P. Smithmaitrie, in *Rehabilitation Engineering*, IntechOpen, **2009**.
[32] P. Smithmaitrie, J. Kanjantoe, P. Tandayya, in *Proceedings of the 1st international convention on Rehabilitation engineering & assistive technology: in conjunction with 1st Tan Tock Seng Hospital Neurorehabilitation Meeting*, **2007**, pp. 174–178.
[33] R. Velazquez, E. E. Pissaloux, M. Hafez, J. Szewczyk, *IEEE Trans. Instrum. Meas.* **2008**, *57*, 1051.
[34] H. Hernandez, E. Preza, R. Velazquez, in *2009 Electronics, Robotics and Automotive Mechanics Conference (CERMA)*, IEEE, **2009**, pp. 402–407.
[35] S. Simeonov, N. Simeonova, *arXiv preprint arXiv:1401.5289* **2014**.
[36] G. C. Bettelani, G. Averta, M. G. Catalano, B. Leporini, M. Bianchi, *IEEE Transactions on Haptics* **2020**, *13*, 239.
[37] I. Balabozov, I. Yatchev, K. Hinov, in *2014 International Conference on Applied and Theoretical Electricity (ICATE)*, IEEE, **2014**, pp. 1–4.
[38] F. Vidal-Verdú, M. J. Madueno, R. Navas, in *Smart Sensors, Actuators, and MEMS II*, vol. *5836*, SPIE, Bellingham, WA, **2005**, pp. 484–492.
[39] P. Chakraborti, H. K. Toprakci, P. Yang, N. Di Spigna, P. Franzon, T. Ghosh, *Sensors and Actuators A: Physical* **2012**, *179*, 151.
[40] Z. Ren, X. Niu, D. Chen, W. Hu, Q. Pei, in *Electroactive Polymer Actuators and Devices (EAPAD) 2014*, vol. *9056*, SPIE, San Diego, California, **2014**, pp. 511–519.
[41] G. Frediani, J. Busfield, F. Carpi, *Medical Engineering & Physics* **2018**, *60*, 86.
[42] Y. Qiu, Z. Lu, Q. Pei, *ACS Appl. Mater. Interfaces* **2018**, *10*, 24807.
[43] W. Makishi, K. Iwami, Y. Haga, M. Esashi, in Technical Digest of the Sensor Symposium, vol. *18*, **2001**, pp. 137–142.
[44] R. Velázquez, E. Pissaloux, M. Hafez, J. Szewczyk, *Applied Bionics and Biomechanics* **2007**, *4*, 57.
[45] N. Besse, S. Rosset, J. J. Zarate, H. Shea, *Adv. Mater. Technol.* **2017**, *2*, 1700102.
[46] I. M. Koo, K. Jung, J. C. Koo, J.-D. Nam, Y. K. Lee, H. R. Choi, *IEEE Transactions on Robotics* **2008**, *24*, 549.
[47] M. Matysek, P. Lotz, T. Winterstein, H. F. Schlaak, in *World Haptics 2009-Third Joint EuroHaptics conference and Symposium on Haptic Interfaces for Virtual Environment and Teleoperator Systems*, IEEE, **2009**, pp. 290–295.

[48] D. N. Karastoyanov, L. A. Doukovska, V. K. Atanassova, in *Proc. of the Third International Conference on Telecommunications and Remote Sensing-ICTRS'*, vol. *14*, **2014**, pp. 88–93.
[49] I. Yatchev, K. Hinov, I. Balabozov, K. Krasteva, *Facta Universitatis-Series: Electronics and Energetics* **2011**, *24*, 157.
[50] H. H. King, R. Donlin, B. Hannaford, in *2010 IEEE Haptics Symposium*, IEEE, **2010**, pp. 95–99.
[51] H. Ishizuka, N. Miki, *Displays* **2015**, *37*, 25.
[52] H. Velasco, How pop its, the tiktok sensation, became the toy of the pandemic., **2021**, https://www.wsj.com/articles/how-tiktok-made-pop-its-the-toy-of-the-pandemic-11629\\291601.
[53] N. H. Runyan, F. Carpi, *Expert Rev. Med. Devices* **2011**, *8*, 529.
[54] D. Pascolini, S. P. Mariotti, *Brit. J. Ophthalmol.* **2012**, *96*, 614.
[55] R. Norton, J. Brown, M. Katzmann, K. Keninger, *Library of Congress, USA* **1994**.
[56] B. Davidovitch, R. D. Schroll, D. Vella, M. Adda-Bedia, E. A. Cerda, *Proceedings of the National Academy of Sciences* **2011**, *108*, 18227.
[57] S. Timoshenko, S. Woinowsky-Krieger, et al., *Theory of plates and shells*, vol. *2*, McGraw-hill, New York, **1959**.
[58] S. P. Timoshenko, J. M. Gere, *Theory of elastic stability*, Courier Corporation, **2009**.
[59] L. D. Landau, E. M. Lifšic, E. M. Lifshitz, A. M. Kosevich, L. P. Pitaevskii, *Theory of elasticity: volume 7*, vol. *7*, Elsevier, Butterworth-Heinmann, Oxford, **1986**.
[60] A. V. Pogorelov, *Bendings of Surfaces and Stability of Shells (Translations of Mathematical Monographs)*, vol. *72*, American Mathematical Society, Providence, R.I., **1988**.
[61] B. Audoly, Y. Pomeau, *Elasticity and geometry: from hair curls to the non-linear response of shells*, Oxford University Press, **2010**.
[62] A. Vaziri, *Thin-Walled Structures* **2009**, *47*, 692.
[63] A. Lazarus, H. C. B. Florijn, P. M. Reis, *Phys. Rev. Lett.* **2012**, *109*, 144301.
[64] D. Vella, A. Ajdari, A. Vaziri, A. Boudaoud, *Phys. Rev. Lett.* **2012**, *109*, 144302.
[65] K. Tan, L. Chen, S. Yang, Q. Deng, *Int. J. Mech. Sci.* **2022**, *230*, 107523.
[66] Z. Zhao, X. S. Zhang, *J. Mech. Phys. Solids* **2022**, *158*, 104628.
[67] A. Abbasi, D. Yan, P. M. Reis, *J. Mech. Phys. Solids* **2021**, *155*, 104545.